


Emergence of Human Oculomotor Behavior in a Cable-Driven Biomimetic Robotic Eye Using Optimal Control

Reza Javanmard Alitappeh , Akhil John , *Student Member, IEEE*, Bernardo Dias, A. John van Opstal , and Alexandre Bernardino , *Senior Member, IEEE*

Abstract—This article explores the application of model-based optimal control principles in understanding stereotyped human oculomotor behaviors. Using a realistic model of the human eye with a six-muscle cable-driven actuation system, we tackle the novel challenges of addressing a system with six degrees of freedom. We apply nonlinear optimal control techniques to optimize accuracy, energy, and duration of eye-movement trajectories. Employing a recurrent neural network to emulate system dynamics, we focus on generating rapid, unconstrained saccadic eye-movements. Remarkably, our model replicates realistic 3-D rotational kinematics and dynamics observed in human saccades, with the six cables organizing themselves into appropriate antagonistic muscle pairs, resembling the primate oculomotor system.

Index Terms—Biologically inspired robots, cable-driven robot, cable pretension, Listing’s law, oculomotor system, optimization and optimal control, recurrent neural network, saccadic eye movements.

I. INTRODUCTION

WITH the increasing use of robots in our daily lives, *biorobotics*¹ is becoming an important topic for researchers in the fields of robotics and biology. Both robots and humans have sensors to perceive the environment and actuators to perform actions. Therefore, designing a control system that allows robots to behave as humans or animals is an important goal in this multidisciplinary research field. In this sense, robots

Manuscript received 6 July 2023; revised 4 January 2024 and 28 February 2024; accepted 7 March 2024. Date of publication 18 March 2024; date of current version 13 August 2024. This work was supported in part by the European Union’s Horizon 2020 program, ERC Advanced Grant, 2016 through project ORIENT under Grant 693400; in part by the Donders Centre for Neuroscience, Radboud University (AJVO); in part by the HAVATAR project (DOI: 10.54499/PTDC/EEL-ROB/1155/2020); and in part by LARSyS funding (DOI: 10.54499/LA/P/0083/2020, 10.54499/UIDP/50009/2020, and 10.54499/UIDB/50009/2020). (*Corresponding author: Reza Javanmard Alitappeh.*)

Reza Javanmard Alitappeh is with the University of Science and Technology of Mazandaran, Behshahr 4851878195, Iran, and also with the Institute for Systems and Robotics (ISR), Instituto Superior Técnico, 1049-001 Lisbon, Portugal (e-mail: RezaJavanmard64@gmail.com).

Akhil John, Bernardo Dias, and Alexandre Bernardino are with the Institute for Systems and Robotics (ISR), Instituto Superior Técnico, 1049-001 Lisbon, Portugal.

A. John van Opstal is with Section Neurophysics, Donders Centre for Neuroscience, Radboud University, 6525 AJ Nijmegen, The Netherlands.

Digital Object Identifier 10.1109/TCDS.2024.3376072

¹Robots inspired by human or animal biological behavior

can be designed to mimic the natural behavior of humans and animals, and biologists can use the results from the artificial models without having to face the ethical and technical difficulties of experiments on the real model. This interdisciplinary work helps roboticists develop better robot designs and control systems [1], but robotics can also be used to explain the emergence of biological behavior [2]. Several such attempts have been published, e.g., on robotic models of cockroaches and hexapedal robots [3], [4], and of insects (such as ants and bees) [4], [5]. Biomimetic robotics has also been applied to biologically equivalent body parts, such as the hand [6] and the eye [7], [8]. Robot models have also been used to study gaze behaviors of humans. Gaze plays an important role in social interactions, signaling one’s attention not only to external events but also to attitudes, affects, or emotions [9].

Optimal control is a paradigm frequently used in the study of neuro-muskuloskeletal systems [10]. However, most of the research focuses on the human biomechanics of the limbs and spine [11]. Only a few studies have proposed the use of optimal control theory in modeling human eye movements [12], [13], [14], [15] but no one has considered the full complexity of the 3-D motion controlled by the six extraocular muscles. In this article, we propose a novel unconstrained biomimetic robotic eye model to study the emergence of the characteristics of human saccadic eye movements. Compared to other works, our contributions in this article are as follows.

- 1) We designed a six DoF cable-driven robot with realistic cable insertions and unconstrained movements.
- 2) We used the model to analyze both the kinematic and dynamic properties of saccades in 3-D.
- 3) The full dynamics of the robotic eye was extracted by training a nonlinear recursive neural network (NARX).
- 4) We show the emergence of humanlike saccades using optimal control to drive the nonlinear robotic eye model.

The article is organized as follows. Section II describes the kinematic and dynamic properties of saccades found in physiology that reflect a tightly coordinated synergy of the extraocular muscles, for which the neuronal control mechanisms are still largely unknown. In Section III, we review other existing robot eye models and show that all lack important mechanical properties to study the emergence of humanlike saccades with similar characteristics as found in physiology. In particular, so far no

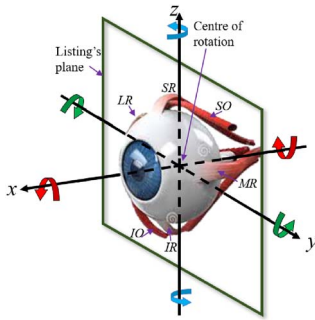


Fig. 1. Representation of the right human eye with its six extraocular muscles. The muscles can rotate the eye in any 3-D orientation around its fixed center of rotation. The right-handed head-fixed reference frame of Listing (arrowheads) shows the three cardinal axes: horizontal (y), vertical (z), and torsional (x), respectively. For example, horizontal recti rotate the eye mainly around the z -axis: lateral rectus, rightward (negative z); and medial rectus, leftward (positive z). In Listing's frame of reference, Listing's plane coincides with the yz plane, and the x -axis points in the so-called primary direction.

studies have presented a model with full 3-D unconstrained saccadic movements actuated by six musclelike actuators. In Section IV, we present our formulation for biomimetic saccade control in robot eyes, following an optimal control approach applied to a suitable simulator of the eye model. In Section V, we describe the mechanical design of our biomimetic eye and its novel characteristics that allow for a study of oculomotor control that is more complete than in other existing models. Sections VI and VII specify the methods used to model and control our system. The results of the simulations are presented in Section VIII, where we show that the proposed approach exhibits properties similar to those found in biology. These properties are not preprogrammed in the system, but emerge from the joint characteristics of our mechanical system and the proposed optimal control laws. Finally, in Section IX we discuss the achievements and directions for future research.

II. HUMAN OCULAR SYSTEM BACKGROUND

This section describes the anatomy and properties of the human oculomotor system that are essential to comprehend and validate our contributions. It also introduces the mathematical notation that will be invoked later.

A. Human-Eye and Extraocular Muscles

The eye is enclosed within a conical cavity, where fat and connective tissues restrict its translation [16], [17]. Thus, the eye can effectively only rotate with three degrees of freedom (DOF) by actuating six extraocular muscles that control its orientation (see Fig. 1). The muscles in the horizontal plane of the right eye, the medial (MR) and lateral (LR) recti, rotate the eye mostly horizontally. The four muscles around the medial plane, the superior (SR) and inferior (IR) recti, along with the sideways pulling superior (SO) and inferior (IO) obliques, enable vertical and cyclo-torsional rotations. It is important to note that the pulling directions of the six muscles are not independent of each other and depend on the orientation of the eye [16]. As illustrated in Fig. 1, any 3-D eye orientation can be

obtained by rotations around the x , y , and z axes, specifying *cyclotorsion*, *pitch*, and *yaw*, respectively. Whereas yaw rotation is achieved by the LR-MR antagonists, pure pitch and cyclotorsional rotations require joint actuation of the four vertical-torsional muscles.

Recordings from primate oculomotor neurons have indicated that, with the eye at rest in the primary position, approximately 65% of the neural population is recruited [18]. Effectively, this means that the eye is kept under continuous pretension and that the neural control for eye movements modulates the relative innervation of agonist and antagonist muscles by changes in firing rates to enable high-precision angular control of the eye. In addition, in a cable-driven robotic system, cables transmit force by applying tension and therefore must remain under tension at all times. To ensure the proper function of a cable-driven robotic eye and to prevent actuator backlash, the six cables must be pretensioned [19]. However, the amount of cable pretension must be adjusted with care: excessive pretension causes more friction, leading to faster wear and tear and shorter lifetime [20]. Insufficient pretension causes slack and deficiency in the control [19].

B. Saccade Kinematics

Typically, humans make about 3–4 saccades per second to scan the visual environment [21] and these are constrained by *Donders' law*, which restricts the rotational degrees-of-freedom of the eyes from three to two [22]. Donders' law states that any eye orientation has a unique cyclotorsional angle, regardless of the path followed by the eye to reach that orientation. It has been argued that Donders' law avoids the problems associated with the noncommutativity of 3-D rotations, which becomes especially important when planning sequences of eye and head movements [23], [24], [25]. *Listing's law* is a further specification of Donders' law. It provides an extra restriction on the eye's cyclotorsion for the special condition with the head upright and still, and the eyes looking at infinity. To describe 3-D eye orientations, the neuroscience literature typically uses the Euler–Rodrigues rotation vector, $\mathbf{r} \equiv \tan(\rho/2) \cdot \hat{\mathbf{n}}$, where $\hat{\mathbf{n}}$ is the unit axis of rotation, and ρ is the rotation angle that brings the eye from the reference orientation at $\mathbf{r} = \mathbf{0}$ to the current orientation [23], [25], [26]. In this representation, Listing's law constrains all eye orientations to Listing's plane, which in the laboratory frame (where $\mathbf{r} = \mathbf{0}$ is straight ahead) is described by $r_x = a \cdot r_y + b \cdot r_z$. A change of coordinates aligns Listing's plane with the (yz) plane, i.e., $r_x = 0$. In Listing's frame of reference, $\mathbf{r} = \mathbf{0}$ is the physiologically defined primary position (Fig. 1). Note that Listing's law holds not only during steady eye fixations but also during smooth-pursuit eye movements and rapid saccadic eye movements. It does not apply to eye-head coordination, static head tilts, vestibular and optokinetic stimulation, or for disjunctive vergence eye movements to fixate nearby targets, for which Donders' law applies [27].

C. Saccade Dynamics

A further important property of saccades is their nonlinear dynamics, described by the so-called *main-sequence* [28].

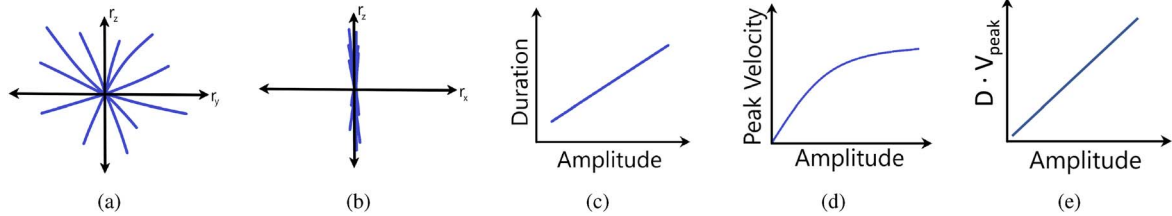


Fig. 2. Schematic illustration of (a) and (b) human saccade kinematics and (c), (d), and (e) nonlinear dynamic properties. (a) and (b) (r_y, r_z) and (r_x, r_z) views of the thin plane formed in 3-D when eye orientations during saccades are represented by rotation vectors (Listing's law: $r_x = 0$). Note nearly straight trajectories in all directions (a). (c) Affine relationship between saccade duration and amplitude. (d) Saturation of peak eye velocities with increasing saccade amplitudes. (e) Linear relation between saccade amplitude and duration times peak eye velocity.

In humans, the peak velocity of the saccade V_{PK} saturates at large amplitudes, A , which follows from the affine increase in the duration of the saccade D , with A : $D = a \cdot A + b$. Because normal velocity profiles are single-peaked, there is a linear relation between A and $V_{\text{PK}} \cdot D$. Fig. 2(c) and 2(d) shows schematic diagrams of these properties. Finally, behavioral experiments have shown that oblique saccade trajectories are approximately straight [29]. As a consequence, the horizontal and vertical component velocities are scaled versions of each other (i.e., they are synchronized), resulting in significant stretching of the smaller component's duration when it participates in an oblique saccade.

III. RELATED ROBOTICS WORK

This section reviews those robotic eye models in the literature that have tried to replicate characteristics found in biology. These models have focused on achieving high movement speeds, or a humanlike external appearance [36], [37], [38], or replicating prerecorded human gaze shifts [39], [40], [41], or hardcoding the biological control rules into the robot control system [42]. However, none of these models studied how the eye movements emerge and how they can be generalized to other designs, as every new design requires a new controller. Furthermore, typical robotic eyes are equipped with only two DOF, usually pan-tilt serial kinematics to control the yaw and pitch of gaze, and cannot independently control ocular cyclotorsion.

Some robotic eye designs made explicit links to the biological oculomotor system and its actuation [7], [30], [31], [32], [43], [44]. Canata and Maggiali [7] developed a mechanical eye driven by four tendons (MAC-EYE). It complied with Listing's law (Section II) by implementing the appropriate routing of the four cables through precalculated pathways. Although a hardwired implementation of Listing's law seems an interesting engineering solution, it does not explain how this property emerges in the human oculomotor system. In [43] and [30], a robotic eye is described, driven by four biologically more realistic contractile muscles. However, the chosen muscle attachments were not similar to those in the human eye. Wang et al. [31] developed a system with six pneumatic artificial muscles (PAMs) with more realistic insertion points, but with the four recti muscles symmetrically arranged, unlike the human recti. The system developed in [32] had six cables with realistic

insertions and pulling directions. However, their eyeball did not rotate around a fixed spherical joint but within a nested gimbal. As the system's inertia changes when moving, it is ineffective for studying saccade dynamics. None of these robotic eyes was used to study oblique saccade trajectories, the *main-sequence* relationships, and underlying muscle-control signals.

Some studies aimed to model the complete complexity of extraocular muscles through simulation [33], [34], [35]. These studies used inverse dynamics or neural activation patterns to drive the simulated eye in a saccadelike way, but they were all limited to 1-D behaviors. Although this may help to understand certain clinical deficits, the complexity of the model impedes the application of different control strategies that could lead to the stereotypical kinematic and dynamic properties of human saccades.

A comparison of previous work on robotic eyes is summarized in Table I. Two of these systems [7], [30] were restricted to four muscles only, and two others [15], [31] did not implement accurate muscle pulling directions. For a proper understanding of the 3-D oculomotor system, however, it is important to model the coupled pulling actions of all six muscles in 3-D, and thus account for the considerable nonlinearities in the system. Although some studies model the human eye in high detail in a simulation environment [33], [34], [35], or with thoroughly scaled physical features [32], they only show saccadelike movements in the horizontal or vertical directions and did not employ the full 3-D coordination of the system, or saccades in oblique directions. To the best of our knowledge, no study modeled the control of the full 3-D system with six muscles to understand the emergence of Listing's Law, the stereotypical *main-sequence* behavior, and straight oblique trajectories of fast saccades.

It has been hypothesized that the brain may optimize a certain cost function, which would lead to the saccadic properties of Fig. 2. However, the application of optimal control theory to understand the emergence of human saccadic behaviors has so far been confined to 1-D [12], or decoupled 3×1 -D models [13]. For example, Saeb et al. [14] studied how open-loop optimal control, combined with a local learning mechanism, could generate eye-head movements in a 1-D linear model.

We recently tested a feedforward open-loop optimal control strategy [45], based on a linear approximation of a simple, but nonlinear, three DOF unconstrained biomimetic robotic eye, which reproduced the 3-D dynamics and kinematics of human saccades [15]. The biomimetic eye had three independent

TABLE I
COMPARISON OF OUR PROPOSAL WITH SIMILAR ROBOTIC EYE SYSTEMS AND SIMULATION MODELS

Model	Control DOF	Muscle Type	Realistic Muscle Insertions	Saccade Directions	Listing's Law	Main-Sequence
MACEYE [7]	4	Cables with motors	✗	✗	Mechanically enforced	✗
Rajendran et al. [30]	4	Contractile muscles	✗	✗	✗	✗
Wang et al. [31]	6	Pneumatic muscles	✗	✗	✗	✗
M. Lakzadeh [32]	6	Cables with motors	✓	1-D	✗	✗
Wei et al. [33]	6	Simulated muscle strands	✓	1-D	✗	✗
Priamikov et al. [34]	6	Simulated Hill-type muscles	✓	1-D	✗	✗
Iskander et al. [35]	6	Simulated Hill-type muscles	✓	1-D	Implemented as constraint	✗
John et al. [15]	3*	Cables with motors	✗	2-D	✓	✓
Our article	6	Cables with motors	✓	2-D	✓	✓

Note: DOF: Degrees of freedom. *The robot in [15] had six muscles but was activated as pairs of hard-coupled motors.

motors, hard coupled to agonist–antagonist cable pairs. The linear approximation for the open-loop controller applied system identification on a physics-based robot simulator. Despite its realistic behaviors, the inherently fixed hard coupling of agonist–antagonistic pairs is an unrealistic feature, which does not explain how it actually emerges in the biological oculomotor system, where the six muscles are independently controlled by their own motor-neuronal nuclei [46], [47], [48], and where agonist–antagonist pairing is a dynamic and flexible strategy that depends on changes in 3-D eye orientation [16], [49], [50].

IV. PROBLEM DEFINITION

We here propose a novel robot design for a realistic six DOF biomimetic eye. To better understand its control and to enable a full characterization of the system, we developed a numerical simulator. Compared to the three DOF model in [15], our new six DOF actuation system brings additional challenges. In particular, the control has to resolve the agonist–antagonist coupling of the muscles and set the appropriate muscle pretensions, which impact on the highly redundant muscular system. For this new system, we developed a controller that replicates most of the kinematic and dynamic characteristics of human saccades, including the emergence of an agonist–antagonist organization of distinct muscle pairs according to the basic optimality criteria.

Similarly to our previous work [15] we take a model-based stance to the control problem, which we divided into two steps: deriving forward models of the mechanical eye, suitable for control design (Problem 1), and computing open-loop optimal control trajectories for the modeled system (Problem 2).

Problem 1 (Approximating the Forward Dynamic Model): To obtain suitable control trajectories with reasonable computational resources, we need to create fast models that approximate the dynamic equations based on nonlinear physics of the cable-driven robotic eye system of Fig. 3. We represent the motor angles as $\mathbf{u} \equiv [u_{IR}, u_{MR}, u_{SR}, u_{LR}, u_{IO}, u_{SO}]^T$ and the six DOF eye state is composed of its 3-D orientation and angular velocity: $\mathbf{x} \equiv [r_x, r_y, r_z, \omega_x, \omega_y, \omega_z]^T$. In [51], we computed linearized approximations of the system equations. However, analytic linearization methods are quite tedious and hard to extend to future model improvements. In this work, we trained a nonlinear neural network model to approximate the system dynamics and used it in the optimization of the control trajectories. The next state of the system \mathbf{x}_{t+1} is predicted from

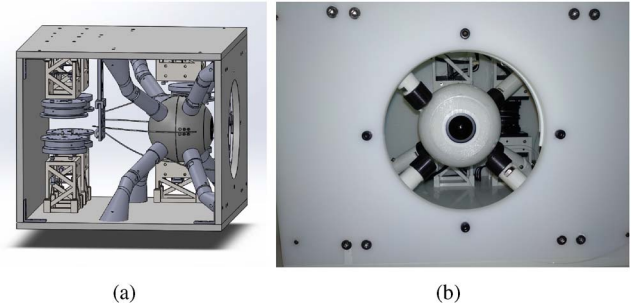


Fig. 3. (a) Schematic 3-D side view of our biomimetic human eye prototype, with six motors (five spindles are visible) independently controlling the six cables (“extraocular muscles”; four are visible) connected to the eyeball. The eye is held in place by eight external arms to allow only 3-D rotations around its fixed center. The ball-contacts of these arms on the eye (not visible) provide a dynamic frictional force that increases the total damping. (b) Front view of the actual mechanical prototype showing the eye with the camera.

the control input \mathbf{u}_t for the six motors and the current state \mathbf{x}_t , where t indicates discrete time. Thus, the model could be defined by the evolution of the state, under the action of the command: $\mathbf{x}_{t+1} = \mathbf{f}(\mathbf{x}_t, \mathbf{u}_t)$.

Problem 2 (Trajectory Optimization): We are attempting to generate saccades that have similar characteristics to those of humans, across the entire 3-D range, by formulating the saccade generation process as an optimization problem with various criteria. The optimal trajectory, $\mathbf{u}_{0:T}^*$, brings the eye from the initial state, \mathbf{x}_0 , to its final state, \mathbf{x}_T , in a finite time-interval, $t \in [0, T]$. If we consider $\mathbf{u}_{0:T} = [\mathbf{u}_0, \mathbf{u}_1, \dots, \mathbf{u}_T]$ as the sequence of input motor commands, then the problem is to find those input motor commands that generate the optimal trajectory at a minimum cost. This cost is typically composed of a linear combination of partial costs on the properties of the trajectory, e.g., duration, accuracy, and energy. The optimal control problem can thus be written as

$$\min_{0 \leq T \leq T_{\max}} \left(\min_{\mathbf{u}_{0:T}} \sum_{t=0}^T C(\mathbf{x}_t, \mathbf{u}_t, T) \right),$$

subject to: $\mathbf{x}_{t+1} = \mathbf{f}(\mathbf{x}_t, \mathbf{u}_t)$, $\mathbf{u}_t \in \mathcal{U}$ (1)

where $C()$ indicates the cost of input state \mathbf{x} and motor command \mathbf{u} for a given duration T , T_{\max} is a bound on the possible values of T , and \mathcal{U} is the set of feasible commands. The optimization process is generally organized in an inner optimization of the motor commands \mathbf{u} for a fixed time horizon T , and an

TABLE II
LOCATIONS OF CABLE INSERTIONS AT EYE AND HEAD

Muscles	IR	SR	MR	LR	IO	SO
Insertion(eye)						
x(mm)	-2	-2	7.7	7.7	-11.2	-11.8
y(mm)	-1.4	0.8	39.3	-39.3	-1.4	-1.2
z(mm)	40	-40	0	0	38.3	-38.1
Insertion(head)						
x(mm)	-100.1	-100.1	-100.1	-100.1	45	45
y(mm)	40.7	40.7	51.6	29.6	37.5	37.5
z(mm)	7.8	-14.9	-3.5	-3.5	62	-62
Length(mm)	111.5	108.8	108.6	127.9	72.3	72.7

outer loop that optimizes T in a certain range $0 \leq T \leq T_{\max}$. Details about the components of the cost function are provided in Section VII.

V. DESIGN OF THE SIX DOF CABLE-DRIVEN ROBOTIC EYE

Fig. 3 shows the 3-D model and the mechanical prototype of our system. Like the human eye, the robotic eye rotates with three DOF around its fixed center whenever the six elastic cables, which represent the extraocular muscles, exert a net torque. Cables are inserted into the globe at contact points (Table II), which were scaled and slightly adjusted from human measurements [52]. Each cable is controlled by its own motor that rotates at a given speed, which pulls the cable around its spindle to exert a torque on the eye. Because cable-pulling directions vary with eye orientation and muscles can only pull (not push), the total system (described below in more detail) is *nonlinear* [15]. Thus, rotating the robotic eye in the same way as the human eye during saccades (i.e., accurately and at high speeds) becomes a highly nontrivial problem.

To study the properties and behavior of the biomimetic eye, we developed a simulator, in which the eye was modeled as a sphere with a fixed center, subject to Newton–Euler’s rigid body equation of angular motion, and actuated by the six cable-driven actuators

$$\alpha = \mathbf{I}^{-1}(\tau_{\text{net}}(\mathbf{x}, \mathbf{u}) - \boldsymbol{\omega} \times \mathbf{I}\boldsymbol{\omega}) \quad (2)$$

where α is the eye’s angular acceleration, \mathbf{I} is the inertia tensor of the eye, \mathbf{u} is the motor configuration of the six motors, $\boldsymbol{\omega}$ is the eye angular velocity, \times denotes the vector (cross) product, and τ_{net} is the net torque on the eye, which depends on the dynamic friction and elasticity torques, τ_d and τ_k ,

$$\tau_{\text{net}} = \tau_k + \tau_d = \sum_{m=1}^6 \tau_m - \mathbf{D}\boldsymbol{\omega}. \quad (3)$$

Here, \mathbf{D} quantifies the eye’s damping matrix, subscript m is the motor index, and the torque exerted by each muscle is as follows:

$$\tau_m = \mathbf{Q}_m \times \mathbf{f}_m \quad (4)$$

where \mathbf{Q}_m is each muscle’s insertion point on the eye, and \mathbf{f}_m is the force applied by each muscle on the eye, which depends on the current state \mathbf{x}_t , goal state \mathbf{x}_G , and control input \mathbf{u}_t .

To simplify the modeling, the cables were approximated by linear elastic springs. The elastic force applied to the eye by

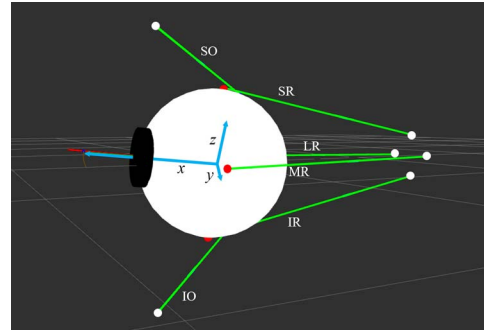


Fig. 4. Visualization of the extraocular muscles (green) for the simulator of the right eye, deviated to the right (red line) from straight-ahead (light blue laboratory frame), where red and white dots indicate insertion points on the eye and head, respectively. Note that the cable pulling directions are not symmetric to the center of the eye, because the insertion points on the head at the back are medially shifted in the $+y$ direction. As a result, the MR muscle is shorter than the LR when the eye is in the primary position.

each cable (\mathbf{f}_m) then depends on its length (l_m), determined by the sum of the length of the cable wound to the motor spindle and the length between the fixed cable head-routing point (white dots in Fig. 4) and the final contact point on the eye (red dots). The length of the cable for each muscle (l_m) varies with the rotation of the motors (\mathbf{u}) and the orientation of the eye (in state \mathbf{x} ; we omit the time index t , for clarity)

$$l_m(\mathbf{x}, \mathbf{u}) = \|\mathbf{Q}_m(\mathbf{x}) - \mathbf{P}_m\| + r_{\text{sp}} \cdot u_m \quad (5)$$

with \mathbf{Q}_m and \mathbf{P}_m the (eye and head) insertion points of cable m , r_{sp} the radius of the spindle, and u_m the rotation angle of the spindle for cable $m \in \{\text{IR}, \text{MR}, \text{SR}, \text{LR}, \text{IO}, \text{SO}\}$. This leads to a dynamic elastic force that is determined by Hooke’s law [53]

$$\mathbf{f}_m = \frac{k}{l_{0m}}(l_m(\mathbf{x}, \mathbf{u}) - l_{0m})\vec{\phi}_m \quad (6)$$

where k is a constant depending on the material and thickness of the cables and l_{0m} is the rest length of cable m . $\vec{\phi}_m$ is the unit vector in the direction of the force applied to the eye.

The inertia of the eye ($\text{diag}(\mathbf{I}) = [4.8, 4.3, 4.8] \times 10^{-4} \text{ kg}\cdot\text{m}^2$), muscle stiffness ($k = 20 \text{ N}$) and damping parameters ($\text{diag}(\mathbf{D}) = [0.04, 0.04, 0.04] \text{ Nm s}$), were selected to closely replicate the biomechanics of the human eye [21]. To implement the constraint that the elastic cables can only pull, the force was set to zero as soon as it went negative. When this happens, the cable loosens and no longer applies tension, a phenomenon known as *slack* (see Section VII-C). Note also that since the constant of elasticity, k , was taken identically for all cables, the effective stiffness varies for movements in different directions. For example, for horizontal movements, the elastic forces are primarily delivered by LR and MR, but vertical movements involve the interaction of SR, IR, SO, and IO.

VI. APPROXIMATIONS OF THE SYSTEM DYNAMICS

The computation of optimal commands through (1) could ultimately be done with nonlinear optimization techniques applied to the nonlinear physics simulator of the eye system.

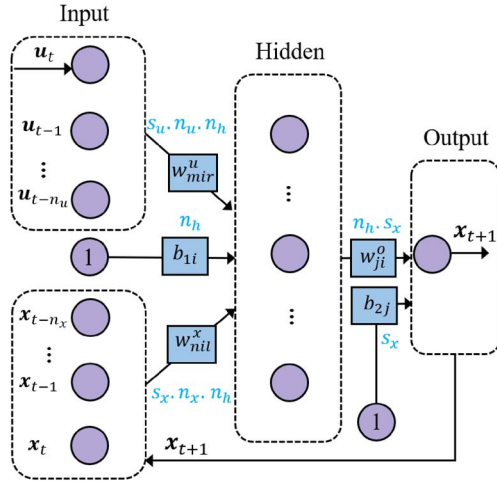


Fig. 5. Architecture of the fully connected NARX model with input, hidden, and output layers. Number of hidden units, $n_h = 55$; input memory: $n_u = 1$; $n_x = 3$; DoF of the state: $s_x = 6$; DoF of the input: $s_u = 6$.

However, running the nonlinear physics simulator in the optimization loop is too time-consuming due to the integration of the nonlinear differential equations. In a previous work, our team explored a local derivative-based linearization of the nonlinear system dynamics, by applying an infinitesimal perturbation method around an equilibrium point [54]. The linear model proved to accurately approximate the nonlinear system for small perturbations around the linearization point, but the quality of the approximation quickly degraded for large saccades. Furthermore, the analytic linearization method involves nontrivial derivatives and does not scale well with physical model complexity. Therefore, in this work, we opt to use a nonlinear data-driven method that learns an approximation of the model from samples of input–output data. This method is much faster to compute than the physics-based simulation and can be adapted to variations of the system by relearning the model after acquiring new input–output data sequences.

The nonlinear autoregressive network with exogenous inputs (NARX) is a type of recurrent neural network [55], [56] that has been applied to model the complex dynamics of nested manipulators [57].

In discretized time, the NARX model can be written as: $\mathbf{x}_{t+1} = f(\mathbf{x}_{t-n_x:t}, \mathbf{u}_{t-n_u:t})$ where the next value of the dependent output signal \mathbf{x}_{t+1} is regressed on previous values of the same output signal $\mathbf{x}_{t-n_x:t}$ and previous values of an independent (exogenous) input signal $\mathbf{u}_{t-n_u:t}$. We have adopted the MatlabTM implementation for the NARX model, illustrated in Fig. 5.

In summary, the NARX model takes the current and past motor commands $\mathbf{u}_{t-n_u:t}$ and the current and past state $\mathbf{x}_{t-n_x:t}$ from the nonlinear system as input to predict the state for the next time step. The size of the network’s memories of control commands and states is $n_u + 1$ and $n_x + 1$, respectively. In Fig. 5, n_h is the number of neurons in the hidden layer; and s_x and s_u are the sizes of the input vectors \mathbf{u} and \mathbf{x} , respectively. $\mathbf{u}_{t-n_u:t}$ and $\mathbf{x}_{t-n_x:t}$ are the (past) inputs to the network. \mathbf{x}_{t+1} is

the output of the network. $b_{1,i}$ and $b_{2,j}$ are the bias weights for the hidden layer and the output layer, respectively. The weight w_{mir}^u connects the input to the hidden layer, w_{jil}^x connects the current and past states to the hidden layer, and w_{ji}^o connects the hidden layer to the output layer ($i \in [1, n_h]$, $j \in [1, s_x]$, $m \in [1, s_u]$, $r \in [1, n_u]$, $l \in [1, n_x]$).

The output of each layer is computed by applying nonlinear (sigmoid) (f_1) and linear (f_2) activation functions, respectively. The biases and weights of the network are adjusted during network training using the *Levenberg–Marquardt backpropagation* technique.

The output of neuron i at time t in the hidden layer $H_i(t)$ is computed by

$$H_i(t) = f_1 \left(\sum_{m=1}^{s_u} \sum_{r=n_u}^0 w_{mir}^u \mathbf{u}_{t-r}^{(m)} + \sum_{j=1}^{s_x} \sum_{l=n_x}^0 w_{jil}^x \mathbf{x}_{t-l}^{(j)} + b_i \right) \quad (7)$$

where the notation $\mathbf{u}^{(k)}$ indicates the k th entry of vector \mathbf{u} . The output of the network is determined by

$$\mathbf{x}_{t+1}^{(j)} = f_2 \left(\sum_{i=0}^{n_h} w_{ji}^o H_i(t) + b_j \right). \quad (8)$$

VII. OPTIMAL CONTROL

A. The Cost Function

Saccades should reach the goal as fast and as accurately as possible, while consuming the least amount of “metabolic” resources, i.e., energy. This leads to the inclusion of three cost functions in the optimal control. In our previous study [15], we did a comprehensive analysis of different combinations of costs and found that the following costs are the most important for generating humanlike saccades.

1) *Duration Cost (J_D)*: *Saccade duration* quantifies the time T , the eye needs to move from initial to final state: the longer, the higher the cost, as saccades should reach the goal in minimum time. The duration cost $J_D(T)$ is defined by a hyperbolic discount function [15], [45], [58]

$$J_D(T) = 1 - \frac{1}{1 + \beta T}. \quad (9)$$

2) *Accuracy Cost (J_A)*: Importantly, the eye should reach the goal state \mathbf{x}_G at time T as accurately as possible, and at zero velocity and acceleration if the target is not moving. We took the accuracy cost J_A as the Euclidean norm of the difference between the final 3-D eye state reached by the controller and the desired goal with zero torsion, $\mathbf{x}_G = (0, G_y, G_z, 0, 0, 0)$. Since the primary position is not known a priori, we expressed the 3-D accuracy cost in laboratory coordinates. We also included a penalty for any state change in a window of $W = 5$ samples as soon as the eye reached the goal at time T

$$J_A(\mathbf{x}) = \sum_{t=1}^W \|\mathbf{x}_G - \mathbf{x}_{T+t}\|^2. \quad (10)$$

3) *Energy Cost (J_E)*: We assume that the total energy consumption by the saccade is proportional to the actuators' angular velocities. As the time steps are uniform, angular velocities can be approximated by differences between angular positions. The energy cost J_E is thus written as [45]

$$J_E(\mathbf{u}) = \sum_{t=1}^T \|\mathbf{u}_t - \mathbf{u}_{t-1}\|^2. \quad (11)$$

B. Controller Design

To reduce the computation effort of the optimization, we represent the sequence of input motor commands $\mathbf{u}_{0:T}$ of a saccade trajectory as a weighted sum of normalized Gaussian basis functions, $\varphi^i(t)$. The configurable number of basis functions N can be much smaller than the number of time steps in the trajectory. Formally,

$$\mathbf{u}_t = \sum_{i=1}^N \boldsymbol{\mu}_i \varphi^i(t), \quad \varphi^i(t) = \frac{\exp\left[-\left(\frac{t-c_i}{h}\right)^2\right]}{\sum_{m=1}^N \exp\left[-\left(\frac{t-c_m}{h}\right)^2\right]} \quad (12)$$

where $\boldsymbol{\mu}_i$ are 6×1 coefficient vectors that will be returned by the optimization process instead of \mathbf{u}_t . For a saccade with duration T , we take $N = \gamma T$ Gaussian basis functions (with $\gamma < 1$ for effective computational reduction), with centers c_i , that are evenly spaced ($\Delta c = T/(\gamma T - 1) \approx \gamma^{-1}$) and with a common standard deviation $h = 2\Delta c$ to ensure good coverage of the temporal dimension. This roughly corresponds to a fixed partition of the duration range.

Defining a $6 \times N$ matrix, $\mathbf{M} = [\boldsymbol{\mu}_1, \dots, \boldsymbol{\mu}_N]$, and a $N \times (T+1)$ matrix, $\boldsymbol{\Phi} = [\varphi_{0:T}^1; \dots; \varphi_{0:T}^N]$, where $\varphi_{0:T}^i$ is the vector with the samples of the i th normalized Gaussian taken at the discrete times, the control trajectory can be written as: $\mathbf{u}_{0:T} = \mathbf{M}\boldsymbol{\Phi}$. Therefore, instead of finding $6 \times (T+1)$ values for a trajectory $\mathbf{u}_{0:T}$, we only need to compute the $6 \times N$ entries from \mathbf{M} , where $N < T$.

The entire trajectory optimization in (1) is done as a bilevel optimization. The duration of the saccade T is optimized in the outer loop of (1). For a selected T , the inner optimization problem can thus be written as

$$\begin{aligned} \mathbf{M}^* = \operatorname{argmin}_{\mathbf{M}} J(\mathbf{x}, \mathbf{u}, T) &= \sum_{\alpha \in \{D, A, E\}} \lambda_\alpha J_\alpha(\mathbf{x}, \mathbf{u}, T) \\ \text{subject to: } \mathbf{x}_{t+1} &= f(\mathbf{x}_t, \mathbf{u}_t), \quad t = 0, 1, \dots, T \\ \mathbf{u}_{0:T} &= \mathbf{M}\boldsymbol{\Phi}, \quad \mathbf{u}_t \geq 0 \end{aligned} \quad (13)$$

where each cost term J_α is multiplied by a fixed weight λ_α and the next state \mathbf{x}_{t+1} is computed by the nonlinear NARX model equation in Section VI. Fig. 6 shows how the trajectory is generated by the inner optimization loop

One of the challenges in optimization is to set appropriate values for the cost weights λ_α . We first estimated the range of candidate values, after which, by trial and error, we manually found the appropriate values for the λ 's.

The optimization procedure, including the inner and outer optimization of (1), is summarized in Algorithm 1. Initially, the

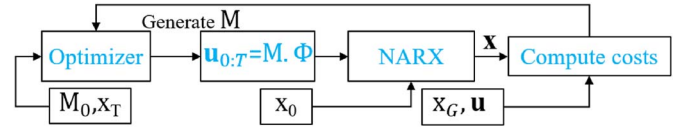


Fig. 6. In the nonlinear optimal control approach, the optimizer generates μ and thus \mathbf{u} as input for the NARX model. From the NARX output, the cost is calculated according to the optimization scheme (13).

Algorithm 1: *Trajectory_Optimization()*

param $\leftarrow \lambda, d, \gamma$ Initialize parameters

Input: $\mathbf{x}_0, \mathbf{x}_G$ Initial and final orientation

for $j = 1$ **to** d **do**

- 1 $T_j \leftarrow j * T_{max}/d$ Saccade duration
 - 2 $N_j \leftarrow \gamma * T_j$ Number of basis functions.
 - 3 $\boldsymbol{\Phi}_j \leftarrow GBF(N_j, T_j)$ Create $\boldsymbol{\Phi}_j$.
 - 4 $\mathbf{M}_j^0 \leftarrow CreateMuZero(N_j)$ Initialize \mathbf{M}_j .
 - 5 $[cost_j, \mathbf{M}_j] \leftarrow Optimize(J(\mathbf{x}_0, \mathbf{x}_G, \mathbf{M}_j^0, \boldsymbol{\Phi}_j, \lambda))$
Optimize cost with given parameters.
 - 6 $[T^*, \mathbf{M}^*, \boldsymbol{\Phi}^*] \leftarrow \min(cost_j)$ Find optimum values.
 - 7 $\mathbf{u}^* \leftarrow \mathbf{M}^* \cdot \boldsymbol{\Phi}^*$ Optimal trajectory.
-

parameters λ , d (number of saccade durations to be evaluated), and γ (ratio of the number of basis functions with respect to the saccade duration in ms) are set. The initial and desired orientations of the eye ($\mathbf{x}_0, \mathbf{x}_G$) are taken as input. Then, for the possible d saccade durations in $0 < T_j \leq T_{max}$, it computes the optimal motor controls and the cost of that solution. Finally, the duration with the lowest cost is the optimal duration T^* .

We applied MATLAB's function *fmincon* with the "sqp" solver to optimize (13). In our experiments, the following values were set: $d = 10$, the maximum number of iterations for the solver was set to 15, and $\gamma = 0.24 \text{ ms}^{-1}$, which corresponds to a separation between Gaussians of about 4.2 ms and a standard deviation of 8.6 ms. These parameters were empirically tuned for a good tradeoff between computational time reduction and accuracy. We further restricted the maximum duration of the saccade to $T_{max} = 210 \text{ ms}$ and initialized all elements of the matrix \mathbf{M} at 2 (corresponding to the resting position and all six motors with fixed pretension).

C. Controlling Pretension

Because of the redundancy in controlling the 3-D orientation of the eye with six motors, the same orientation can be achieved by (infinitely many) different motor-angle combinations, as the amount of cocontraction of antagonistically acting muscles is undetermined. Therefore, an important feature to control is the amount of pretension (the set of initial motor angles), such that the eye is able to reach any orientation in the oculomotor range without the cables going slack during eye movements. Therefore, we optimized the initial motor angles (\mathbf{u}) such that their squared norm is minimal, under the constraints that ensure

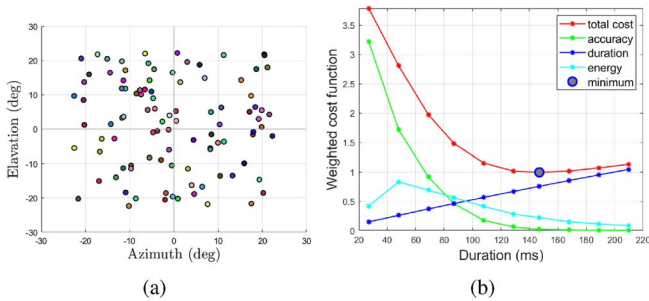


Fig. 7. (a) Ninety-nine oblique goal directions as azimuth (rightward positive) and elevation (upward positive) angles in the amplitude range from 5° to 30° , as used for the zero-initial and continuous saccade tests in our experiments. (b) Cost functions for a rightward horizontal saccade of 22° starting from the origin in the trajectory optimization procedure, evaluated at ten discrete time steps. The large blue dot indicates the minimum total cost of the trajectory and is found at $T = 147$ ms.

positive cable forces in equilibrium state \mathbf{x} , while the total elastic torque in the system is zero [(3) and (6)]:

$$\begin{aligned} \min_{\mathbf{u}} \quad & \|\mathbf{u}\|^2 & \mathbf{f}(\mathbf{x}, \mathbf{u}) &> 0 \\ \text{subject to} \quad & & \tau_k(\mathbf{x}, \mathbf{u}) &= 0 \\ & & \mathbf{u}_{\text{agonist}} + \mathbf{u}_{\text{antagonist}} &> 2\theta \end{aligned} \quad (14)$$

where \mathbf{f} is the tension at each cable, τ_k is the total torque resulting from the cable tensions, and θ is a minimum bound for the average motor angle for the three antagonistic motor pairs ($\mathbf{u}_{\text{agonist}}$ and $\mathbf{u}_{\text{antagonist}}$). These pairs are MR-LR, IR-SR, and IO-SO. The value of θ is a user-defined parameter that depends on the radius of the spindle around which the cables are wound and should be chosen as the lowest value for which the cables would not move slack throughout the trajectory.

Note that we did not control for slack explicitly at runtime. Our strategy to prevent slack was to empirically tune the pretension of the tendons such that we would not observe slack in a set of large saccades. As we have not verified the existence of slack in all other saccades tested, we cannot theoretically ensure the absence of slack for all cases.

VIII. SIMULATION RESULTS

To evaluate our approach, we analyzed and compared several output parameters of the system regarding the 3-D kinematic (Listing’s plane) and dynamic (velocity profile) behavior (Fig. 2), and the “neural” control signals from the six motors.

A. Simulation Setup

To evaluate our controller on saccades of different amplitudes and directions, we created a test set of 99 random target locations in horizontal, vertical, and oblique directions with amplitudes between 5° and 30° from straight-ahead [Fig. 7(a)]. We performed two saccade sequences: a *zero-initial* sequence, where every saccade started from the origin ($[0, 0, 0]$), and a *continuous* sequence, where the next saccade started from the final orientation of the previous saccade, and so on. All simulations were performed in MATLAB 2021 on a laptop with Windows 10 operating system, 16 GB Ram and a CPU core i7.

The weights λ_α of the three cost functions, J_α in our optimization (13) were manually calibrated with the aim to achieve humanlike dynamic characteristics for the eye system: $\lambda_A = 1$, $\lambda_D = 0.04$, and $\lambda_E = 0.002$. Fig. 7(b) shows an example of the behavior of the three costs for a 22° horizontal saccade, together with the total cost (red), executed for ten different saccade durations between 30 and 210 ms. The optimal saccade duration T is found at the minimum of the convex total cost curve, that is, at $T = 147$ ms.

As for the setting of the cables’ pretensions discussed in Section VII-C, we found by trial and error that values of θ around 2 rad (14) worked well for all saccades.

B. Model Learning

To train the NARX network, we have acquired a large sequence of input–output data sampled at a frequency of 1 ms. We have followed the approach of [15] and generated for input data independent pseudorandom binary signal sequences (PRBSs) [59], typically used in system’s identification. PRBS is a deterministic signal composed of rectangular pulses of fixed amplitude but variable duration that has properties similar to those of white noise (flat spectrum). Thus, it equally excites all frequencies of interest in the system. The amplitude range of these signals was chosen to obtain good approximations of the model output in the range of the desired saccade amplitudes.

The total data length is 2×10^6 ms, which covers a wide range of the workspace (Fig. 8). For computational reasons, we reduced the data size by downsampling the signals to 3 ms time intervals.

By feeding the dataset to the NARX model, the best result was achieved after 96 training epochs with $\text{MSE} = 0.0018$ (rad^{-2})². Fig. 8 shows the result of the trained NARX network (red line), tested on a random set of eye movements (blue trace), which verifies how well the network learned the forward dynamics of our nonlinear robotic eye model.

C. Kinematic Behavior

To study the 3-D kinematics of the eye movements resulting from our controllers, we analyzed the amount of cyclotorsion of the 3-D trajectories with respect to Listing’s plane. Fig. 9(a) shows the result of the continuous saccade test in the laboratory xy plane (black). Note that Listing’s plane is, typically, not aligned with the vertical axis of the head frame. The data (red) were therefore rotated around the z -axis (after calculating the best-fit plane) to align them with Listing’s frame of reference [cf. Fig. 2(b)].

Table III presents the standard deviations of cyclotorsion around Listing’s plane for different amplitude ranges and saccade tests. These values correspond well with the range reported for monkey and human eye movements (between 0.6° and 1.0°) [23], [25].

Fig. 9(b) shows the eye-movement trajectories in Listing’s yz plane. Overall, the eye-movement trajectories appear quite straight.

To better quantify this observation, we calculated curvature C as the maximum absolute deviation d_{\max} of the trajectory

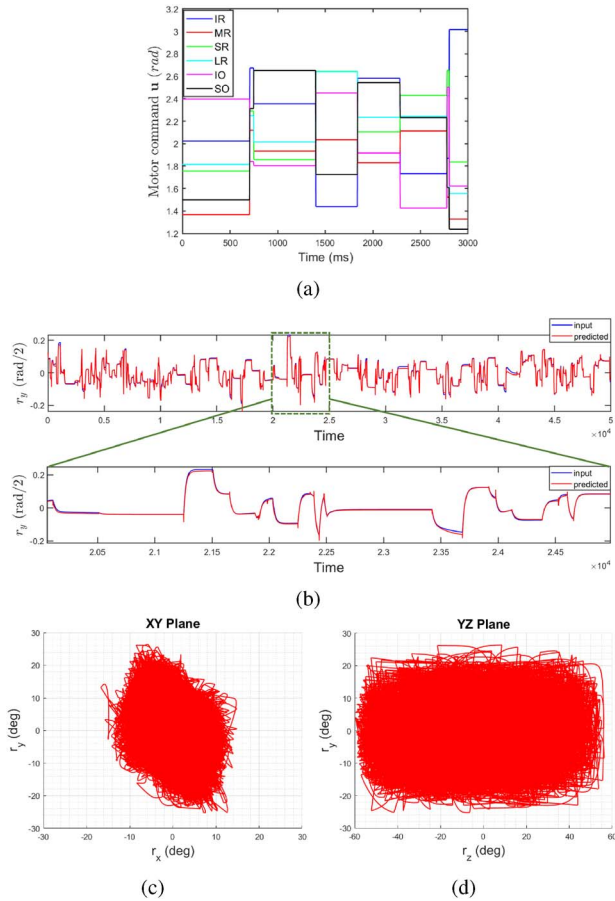


Fig. 8. (a) Illustrative selected section of random motor responses over 3000 ms (out of 2×10^6 ms), which served as a training set for the NARX network. Motor commands are within the range [0–3] rad. (b) Eye orientation along the y -axis for a sample input signal (blue trace) of 50 000 samples (150 000 ms) and the predicted signal (red) for the trained NARX model. Inset: Same data on an expanded scale. Root mean squared error (RMSE) = 0.06 rad^{-2} and $r^2 = 0.97$ between data and prediction, indicating an excellent approximation. (c) and (d) Rotation vector components (in degrees) in the (xy) (c) and (yz) (d) planes of the corresponding 3-D eye orientations in the laboratory frame (subsample of the total dataset). Note that the $r_x r_y$ range of the system is smaller than the r_z range and that the data are slightly tilted in the xy plane.

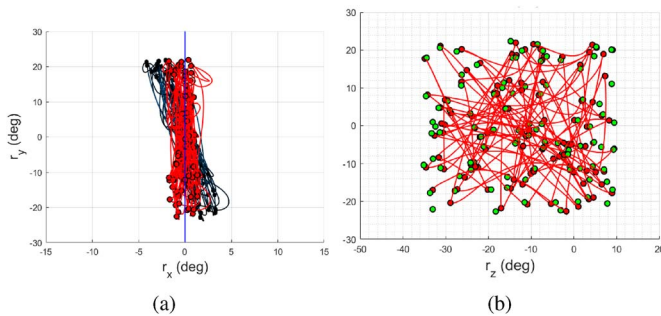


Fig. 9. (a) xy and (b) yz projections of 3-D eye-movement trajectories in Listing's coordinates (red) from the continuous saccade sequence. Black: xy data in the laboratory frame before applying a rightward rotation of 18.11° about the z -axis into Listing's coordinates. The blue vertical line at $r_x = 0$ indicates Listing's plane after rotation. Green dots in (b) correspond to the actual (rotated) goals of the saccade set in Listing's frame (note different scales for the abscissas).

TABLE III
STANDARD AND MAXIMUM DEVIATION OF THE LISTING'S PLANE

Saccade/ Control	Saccade Amplitude $^\circ$	Deviation (STD, Max) $^\circ$
Zero-initial	< 10	0.12, 0.35
	< 20 & ≥ 10	0.24, 0.77
	< 35 & ≥ 20	0.36, 1.35
Continuous	< 10	0.52, 1.24
	< 20 & ≥ 10	0.54, 2.1
	< 35 & ≥ 20	0.85, 2.8

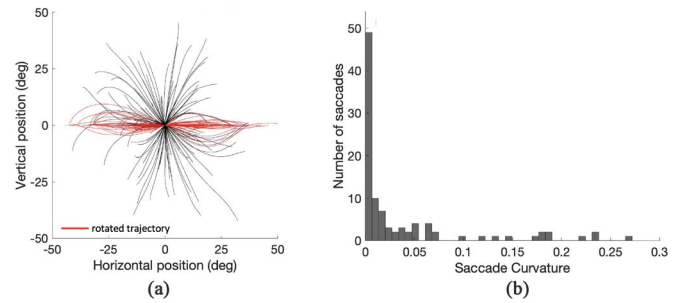


Fig. 10. (a) Movement trajectories in vertical and horizontal direction for the 99 saccades of the random sequence, all aligned in (0,0) (black), and after their rotation onto the horizontal axis (red). (b) Distribution of curvature values for all 99 saccades. The far majority of saccades is straight ($C < 0.03$).

TABLE IV
CORRELATIONS: MUSCLE COMMANDS AND VELOCITY COMPONENTS

	Antagonists			Agonists		Saccade
	LR-MR	SR-IR	SO-IO	SR-IO	SO-IR	$\omega_H - \omega_V$
μ	-0.88	-0.89	-0.49	+0.73	+0.73	0.80
σ	0.12	0.22	0.42	0.24	0.33	0.29
mode	-0.95	-0.99	-0.95	+0.91	+0.94	0.96

from the straight vector connecting the start- and end points in the yz -plane, normalized by its vector length: $C \equiv d_{\max}/|A|$ (e.g., for a semicircular trajectory, $C = A/(2A) = 0.5$) [60]. In Fig. 10(a), we show the set of continuous saccades of Fig. 9 after subtracting their starting points such that all trajectories align with the origin. Then, by rotating the trajectories to the horizontal axis the curvature simply becomes the following:

$$C = \frac{\max(|v_t|)}{|h_{\text{end}} - h_{\text{start}}|}$$

with v and h the vertical and horizontal coordinates of the rotated trajectory, respectively. Fig. 10(b) shows the distribution of saccade curvatures C . We divided saccades into two main categories: straight ($C < 0.03$) versus substantially curved ($C > 0.1$), and found that 70/99 saccades were straight, with only 6/99 substantially curved. This small group of curved saccades was generated from eccentric initial positions with saccade vectors not directed toward the center of the oculomotor range.

The straightness of saccade trajectories requires that the horizontal/vertical components of their velocity profiles are scaled: $\omega_H(t) \propto \omega_V(t)$. We indeed found high correlations (for the continuous saccade set: $\mu = 0.80$, $\sigma = 0.29$, see Table IV). As curvature was not explicitly included as a cost in our algorithm, this apparent cross coupling in eye behavior is an emerging

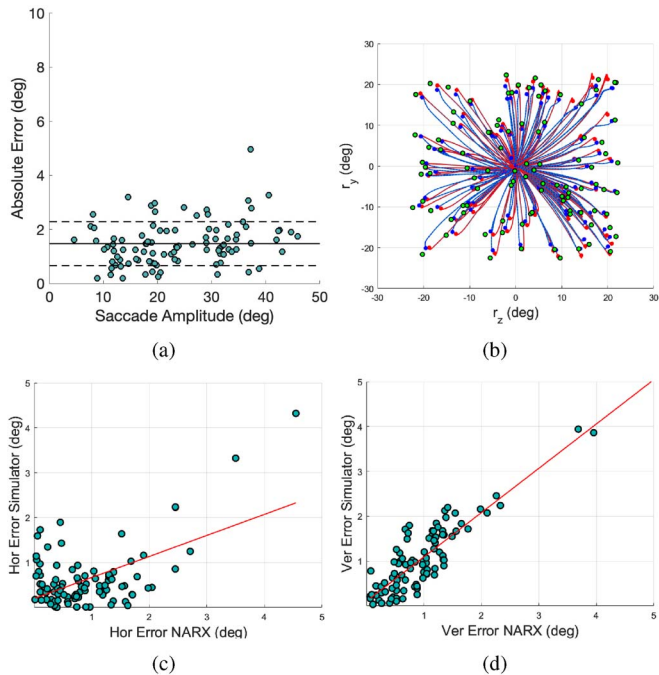


Fig. 11. Accuracy. (a) Absolute localization errors (distance between target and saccade endpoint), here shown for the continuous saccade set versus the saccade amplitude of the nonlinear simulator. Note that errors do not systematically increase with saccade size. Mean error: 1.47° (σ : 0.81°). (b) yz plane of the zero-initial saccade trajectories for the nonlinear simulator (red) and NARX model (blue). Green dots are the target points. Note the similarity between the two approximation methods. (c) Comparison of the endpoint localization errors of the horizontal target component generated by NARX and simulator. (d) Comparison of the localization errors for the vertical target components. Note that the errors are small (typically $< 2^\circ$) and quite comparable for the two approximation methods.

property of the optimal control strategy. However, this also must indicate a considerable amount of cross coupling between the six motors, despite the fact that they are physically independent of each other.

D. Saccade Accuracy

The absolute localization error of the saccades resulted to be independent of their amplitude and was on average 1.47° [σ : 0.81° ; see Fig. 11(a); data from the nonlinear simulator]. The relative error (absolute error normalized by amplitude) thus decreased with the saccade amplitude, in contrast to what has been reported for results obtained from human saccades [61] (see Section IX).

To analyze the source of the localization errors, we compared the accuracy of the solutions for the optimal trajectories obtained with the NARX model with those from the nonlinear simulator. As the nonlinear simulator represents the actual physical plant, any errors in the accuracy of the end points must be due to the tradeoff between *accuracy*, *duration*, and *energy*, expressed in the optimization cost function (apart from numerical errors). The results are illustrated in Fig. 11.

Fig. 11(b) shows the oblique saccade trajectories for the zero-initial dataset in laboratory coordinates for the simulator (red) and NARX (blue), which shows that, despite some small

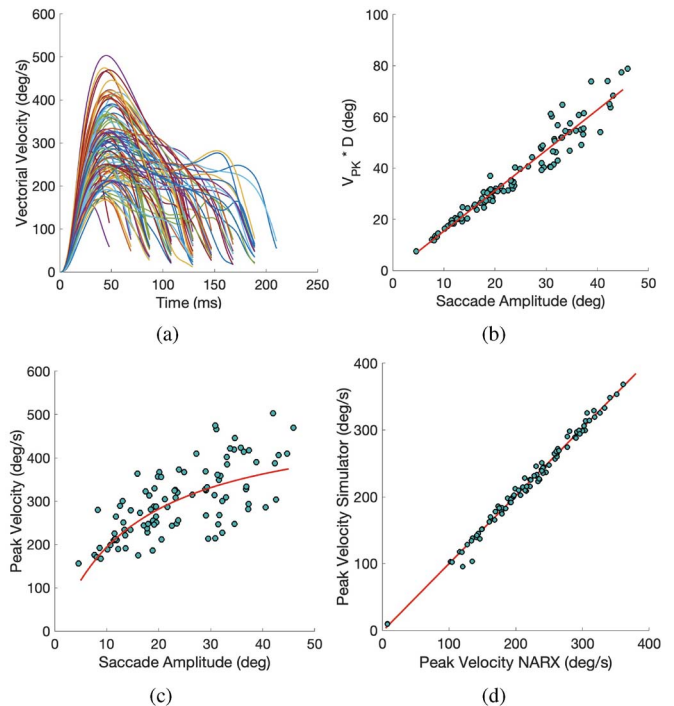


Fig. 12. Dynamics. (a) Vectorial velocity profiles of the continuous saccade set. (b) Amplitude A versus $V_{PK} \cdot D$ (in degrees). Note the very tight linear relationship ($r^2 = 0.94$), with an offset of $c = -0.47^\circ$ and a slope of $d = 1.58$. (c) $A - V_{PK}$ relation saturates for large saccades. The red line follows from the affine $A - D$ relation (with an offset at $a = 0.048$ s and a slope $b = 0.0031$ s/deg; r^2 : 0.72; not shown) and the regression in (b). All data in (a)–(c) are from the continuous set generated by the nonlinear simulator. (d) Peak eye velocity for the NARX model versus the nonlinear simulator (zero-initial set) indicates that both approximations yielded similar dynamics: offset: -1.7 deg/s, slope: 1.02, and r^2 : 0.99.

nonsystematic discrepancies, the trajectories are highly similar. The green dots show the target locations. Fig. 11(c) and 11(d) compares the horizontal and vertical localization error components for the two approximation methods. Both methods yielded small errors (typically below 2°), and both component errors were correlated.

Overall, the NARX model provided a good approximation for the nonlinear physics-based simulator and did not add systematic errors to the accuracy of the solution.

E. Saccade Dynamics

Fig. 12(a) shows the vectorial velocity profiles for all saccades of the continuous dataset from the nonlinear simulator. Most velocity profiles were single-peaked, with some exceptions for very large eye movements that were generated from eccentric initial eye orientations. These velocity profiles, reaching peak velocities near 500 deg/s, qualitatively resemble those seen in human data (e.g., [29] and [62]; see Section IX).

Fig. 12(b) quantifies the *main-sequence* property of saccade amplitude A versus $V_{PK} \cdot D$, for the continuous saccade set [cf. Fig. 2(e)], showing a strong linear relationship, and expressing the fact that most velocity profiles were indeed single-peaked.

Because of the affine dependence of saccade duration on amplitude [Fig. 2(c)], the peak velocity is expected to saturate for

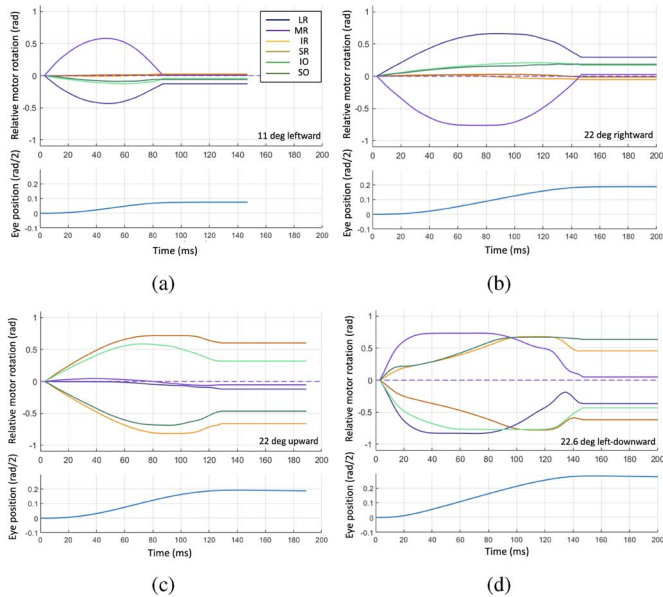


Fig. 13. Changes in motor-command angles (in rad) re. pretension for the optimal trajectory of (a) an 11° leftward and (b) a 22° rightward saccade, (c) a 22° upward, and (d) a left-downward oblique saccade to $[22.6^\circ, 22.6^\circ]$, all from straight ahead. Note that motors form antagonistic muscle pairs with pulse-step/antipulse-step behaviors. Note also the different control dynamics for horizontal versus vertical/torsional systems and the upward action of IO in the vertical saccade. The six muscles contribute to the oblique saccade. Real pretension values were $[2.01, 1.96, 1.98, 2.03, 1.97, 2.02]$ rad. Lower panels: vectorial eye position (rad^{-2}).

large saccade amplitudes, which is shown in Fig. 12(c), where the solid red line is the predicted relation based on the regression in panel (b) and the $A - D$ relationship. It is described by

$$V_{\text{PK}}(A) = \frac{c + d \cdot A}{a + b \cdot A} = \frac{-0.47 + 1.58 \cdot A}{0.048 + 0.0031 \cdot A} \text{ deg/s}$$

which asymptotes at $1.58/0.0031 \approx 510$ deg/s.

We also compared the saccade dynamics of the two approximation methods by comparing the peak velocities of their respective trajectories. Fig. 12(d) shows that the peak velocities were strongly correlated ($r^2 = 0.993$), and highly similar (slope of the regression line: 1.016).

Note that the *main-sequence* relation of the system [Fig. 12(c)] shows considerable variability in the peak velocity for a given amplitude. Part of this variability, which is also observed in human oblique saccades [29], is due to the strong-direction dependence of the saccade dynamics, and the variation in initial conditions, as these invoke different muscle synergies that significantly influence movement speed. How these synergies are formed is described next.

F. Analyzing Muscle Forces

Fig. 13 shows the changes in the instantaneous motor control angles of the six tendons for four saccades starting from the center. Several interesting observations can be made. First, pure horizontal saccades [Fig. 13(a) and 13(b)] only involve activation of the tendons m_{MR} and m_{LR} , while vertical saccades require joint action of the vertical recti and obliques [Fig. 13(c)].

For oblique saccades [Fig. 13(d)], all six tendons are activated. Second, motors act in antagonistic pairs for all saccades, since the main activation controls of the involved muscles are in opposite directions [16], [48], [63]. Third, control of the eye tendons can be characterized as a *pulse-step* activation for the agonists, and an *antipulse/negative step* for the antagonists [21]. Fourth, the positive and negative pulses of the activated agonists and antagonists exactly match the saccade durations, whereas the agonists and antagonist postsaccade steps attain increased and decreased values relative to the initial pretensions, respectively. Finally, the pulse (and antipulse) amplitudes increase with saccade amplitude. Thus, the net force on the right eye for a rightward horizontal saccade is delivered by the m_{LR} , together with an equally rapid relaxation of the m_{MR} , while the other four tendons stay close to their equilibrium pretension values; the slight change in the obliques' tension during larger horizontal saccades is systematic (but note that their net effect is zero). Similarly, an upward saccade requires joint activation of the m_{SR} , m_{IO} muscles and a simultaneous inactivation of the m_{IR} , m_{SO} muscles, and vice versa for a downward saccade, without change in net tension for the horizontal recti [Fig. 13(c)]. Note that all these properties emerged from the optimal control strategy. Interestingly, all have been observed in neurophysiological recordings from monkey oculomotor neurons [16], [18], [46], [47], [48], [63].

Table IV summarizes the correlation statistics between the five different muscle pairs, grouped as antagonists and agonists, respectively [e.g., Fig. 13(d)], for all oblique saccade trajectories in the continuous paradigm with a direction at least 20° away from pure horizontal or vertical ($N = 57$ saccades). Note that the antagonists have their correlation modes close to -1.0 , and the agonists close to $+1.0$. Note also that the SO-IO muscle pair (antagonists for cyclo-torsion) is more variable than the other four pairs, which is due to Listing's law that strongly restricts the torsional range in the saccades. The rightmost column shows the correlation statistics of the horizontal and vertical velocity profiles of these oblique saccades. The mode near 1.0 indicates that most trajectories were virtually straight.

IX. DISCUSSION

A. Summary

We developed a physics-based model for a biomimetic robotic eye with six independent motors controlling elastic strings, mimicking human eye movement (Fig. 1) by rotating the eye around its fixed center with three DOF (Fig. 8). The nonlinear system dynamics were learned using a recurrent neural network under optimal control. Our study shows that the control system efficiently produces humanlike 3-D eye rotations with appropriate saccade characteristics (Figs. 2, 9, 11, 12, and 13). Further details on these properties are discussed as follows.

B. Nonlinear Approximations and Pretension

Pretension in tendons corresponds to a low static cocontraction of eye muscles in the primate oculomotor system [16], [21]. Despite low reported cocontraction, all eye-muscle neuronal

pools exhibit a net neural activity for all static eye positions [18], [21], [46], [48]. This net activity, though not subjected to unexpected loads or gravity, may facilitate fine control of eye orientation by modulating firing rates and overcoming static friction [21]. The push–pull organization with static pretension thus enhances angular resolution. In the nonlinear NARX model, only pretensions for the central equilibrium orientation were set, ensuring a convex total cost function through trial and error [Fig. 7(b)]. The model is flexible for future complexities and can be applied to directly control a physical robotic eye without explicit mathematical approximations of its physics.

C. Straight Trajectories

Eye-movement trajectories in the yz plane were straight, despite distinct dynamics for horizontal and vertical saccade components (Fig. 9) and independent control of the six motors. Straight saccades indicate highly correlated velocity profiles, with one component influencing the other [29]. As a consequence, the control signals for the six motors are strongly coupled, dependent on initial eye orientation and target coordinates. The optimal control, emphasizing minimum time to reach the goal (J_D), leads to single-axis rotations by organizing the six motors into a central 3-D vectorial eye-velocity generator.

A subset of saccades with higher curvature and lower synchrony likely results from system nonlinearities at large eccentricities and a tradeoff in the optimal control objective. Although curvature was not explicitly considered in our optimization, movement duration and accuracy cannot both be optimally satisfied simultaneously. Interestingly, similar curvature is observed in saccadic eye movements in humans and monkeys [60], [62]. Our study offers a quantitative and mechanistic explanation for this observed property.

D. Nonlinear Main-Sequence Dynamics

The main-sequence behavior of human saccades is replicated in our biomimetic system (Fig. 12). These nonlinear dynamics primarily arise from optimal control implementing a speed-accuracy tradeoff, rather than from plant nonlinearities [12], [15], [45]. That saccade duration increases with amplitude is already evident in matching pulse/antipulse durations of antagonistic motors (Fig. 13). Observations indicate that saccade velocity profiles are positively skewed, with skewness increasing with amplitude [64]. Our simulations also reflect this property to some extent [Fig. 12(a)], as single-peaked velocity profiles reach their peak at approximately the same time for all amplitudes (for zero-initial saccades: mean 50 ms, std 14 ms). Skewness in our data (time-to- V_{PK} divided by saccade duration) negatively correlates with amplitude ($r = -0.4$).

E. 3-D Kinematics

Also Listing’s law emerged from the applied optimal control. Although the accuracy cost restricted torsion of the final goal orientation to zero, the optimal control resulted in a tilted plane for the full trajectories in the laboratory frame [Fig. 9(a)].

A minor 18-degree leftward rotation around the z -axis aligned the data with Listing’s frame. The slight asymmetry in our robotic eye’s muscular geometry, such as $l_{MR} < l_{LR}$, was incompatible with Listing coordinates at zero torsion. This asymmetry was also evident in the xy projection of the training data (Fig. 8). Our previous work [15] demonstrated that Listing’s law could automatically emerge by including total fixation force as a fourth cost, systematically tilting the plane in the xz plane after displacing vertical/torsional muscles along the y -axis. We propose that the orientation of Listing’s plane and primary position direction result from the specific geometrical arrangement of muscle insertions on the eye and head, combined with their relative lengths and elastic properties.

F. Antagonistic Organization

The joint antagonistic activation patterns of the six muscles (Fig. 13) emerged from the optimal control strategy in our model. A horizontal rightward saccade involves a fast contraction (pulse) of the LR muscle and synchronous relaxation (antipulse) of the MR muscle, generating the movement with minimal extra cocontraction [Fig. 13(a)]. Similarly, a purely vertical upward saccade arises from rapid synchronous contraction of SR/IO agonists and relaxation of IR/SO antagonists, maintaining equilibrium pretension in horizontal muscles [Fig. 13(b)]. Oblique saccades exhibit complex antagonistic interactions between all six tendons [Fig. 13(c)].

These emerging synergies align with the pulling directions of each muscle [16], embodying the known “push–pull” organization of the oculomotor and vestibular systems, and reflecting Sherrington’s principle of reciprocal innervation [65]. The pulse-step innervations of antagonistic muscle pairs closely resemble their neurobiological counterparts of primate oculomotor neurons [16], [18], [46], [47], [48], [63], reflecting the biomimetic eye’s built-in property as an overdamped (nonlinear) filter due to velocity-dependent dynamic friction [66].

G. Limitations and Further Study

Physics-based simulations are important in advancing our understanding of how movement is controlled. They allow fast and easy exploration of different types of control and system characteristics. However, some aspects can only be realized with real robotic implementations. For this purpose, we have designed and built a robotic spherical eye actuated by six motor driven cables with realistic pulling directions to mimic the six extraocular muscles [67]. Despite the challenges in performing large-scale experiments, the current prototype exhibits the ability to perform a wide range of eye movements with the appropriate characteristics and will be used in future work to validate the computer simulations. Furthermore, by building mechanical prototypes we can realize what the key characteristics are to include in computer simulations. The simulator (Fig. 4) produced realistic humanlike saccades and neural control signals but involved simplified approximations compared to the actual robotic system (Fig. 4). Improvements can be made by incorporating more neurobiological and physical realism.

First, the tendons are attached to a fixed point on the globe and their paths may pass through the peripheral rim of the eye. More realistically, tendons should wrap around the globe, adjusting their paths as a function of 3-D eye orientation. In the primate eye, muscle trajectories are partially fixed to the sclera [50], influencing effective pulling directions that may be further modified by pulleys. Additionally, eye muscles consist of multiple fibers, not a single tendon (Fig. 1), which may further affect iso-innervation trajectories and 3-D plant characteristics [16], [48].

Second, our simulations lacked additive and multiplicative noise in control, impacting velocity profile shapes (skewness) and potentially removing the need for an energy cost [12], [45], [68]. Including multiplicative noise may also better align error patterns [Fig. 11(a)] with human behavior, where errors increase linearly with saccade amplitude.

Finally, we imposed a 3-D constraint on movement accuracy that explicitly incorporated Listing's law and the primary position. In our previous work [15], a 2-D accuracy cost and a minimized total fixation force sufficed to show how Listing's law related to muscular geometry. With six independent motors, specifying pretension was necessary. Designing a quadratic fixation cost, combined with the previous two points, may allow the optimal control to generate Listing's law, the primary position, and specify optimal muscle pretension at each eye orientation—an area for future exploration.

X. CONCLUSION

This article has demonstrated how model-based optimal control principles can explain stereotyped human oculomotor behaviors, through simulations in a realistic model of the human eye with a cable-driven actuation system that mimics the six DOF of the extraocular muscles. Previous work has addressed only systems with one to three DOF. This article is the first study of a six-muscle system design, which introduced novel challenges. We proposed nonlinear optimal control techniques to optimize the accuracy, energy, and duration of eye movement trajectories, and we used a recurrent neural network that learned to emulate the nonlinear system dynamics from the recorded sample trajectories. We showed that realistic 3-D rotational kinematics and dynamics, as seen in human saccades, emerged from our model and that the six cables organized themselves into appropriate antagonistic muscle pairs, as in the primate oculomotor system. This research has demonstrated the potential of robotic models to test theories on the behavior of humans or animals and to help understand many aspects of intelligence and control in natural systems.

REFERENCES

- [1] D. Lambrinos, H. Kobayashi, R. Pfeifer, M. Maris, T. Labhart, and R. Wehner, "An autonomous agent navigating with a polarized light compass," *Adapt. Behav.*, vol. 6, pp. 131–161, 1997.
- [2] B. Webb, "Can robots make good models of biological behaviour?" *Behav. Brain Sci.*, vol. 24, pp. 1033–1050, 2001.
- [3] J. Lee, S. N. Sponberg, O. Y. Loh, A. G. Lamperski, R. J. Full, and N. J. Cowan, "Templates and anchors for antenna-based wall following in cockroaches and robots," *IEEE Trans. Robot.*, vol. 24, no. 1, pp. 130–143, Feb. 2008.
- [4] S. Sponberg and R. J. Full, "Neuromechanical response of musculo-skeletal structures in cockroaches during rapid running on rough terrain," *J. Exp. Biol.*, vol. 211, pp. 433–446, 2008.
- [5] J. Stankiewicz and B. Webb, "Looking down: A model for visual route following in honey bees," *Bioinspiration Biomimetics*, vol. 16, no. 5, 2021, Art. no. 055007.
- [6] Z. Lyu and Q. Xu, "Design of a new bio-inspired dual-axis compliant micromanipulator with millimeter strokes," *IEEE Trans. Robot.*, vol. 39, no. 1, pp. 470–484, Feb. 2023.
- [7] G. Cannata and M. Maggiali, "Models for the design of bioinspired robot eyes," *IEEE Trans. Robot.*, vol. 24, no. 1, pp. 27–44, Feb. 2008.
- [8] E. Maini, G. Teti, M. Rubino, C. Laschi, and P. Dario, "Bio-inspired control of eye-head coordination in a robotic anthropomorphic head," in *Proc. 1st IEEE/RAS-EMBS Int. Conf. Biomed. Robot. Biomechatron. (BioRob)*, 2006, pp. 549–554.
- [9] M. Argyle, R. Ingham, F. Alkema, and M. McCallin, *The Different Functions of Gaze*. Berlin, Germany: Walter de Gruyter, 1973.
- [10] T. V. Wouwe, L. H. Ting, and F. D. Groote, "An approximate stochastic optimal control framework to simulate nonlinear neuro-musculoskeletal models in the presence of noise," *PLOS Comput. Biol.*, vol. 18, no. 6, 2022, Art. no. e1009338.
- [11] A. Bersani, G. Davico, and M. Viceconti, "Modeling human suboptimal control: A review," *J. Appl. Biomech.*, vol. 39, no. 5, pp. 294–303, 2023.
- [12] C. M. Harris and D. M. Wolpert, "The main sequence of saccades optimizes speed-accuracy trade-off," *Biol. Cybern.*, vol. 95, pp. 21–29, 2006.
- [13] R. J. van Beers, "Saccadic eye movements minimize the consequences of motor noise," *PLoS One*, vol. 3, pp. 1–8, 2008.
- [14] S. Saeb, C. Weber, and J. Triesch, "Learning the optimal control of coordinated eye and head movements," *PLOS Comput. Biol.*, vol. 7, 2011, Art. no. e1002253.
- [15] A. John, C. Aleluia, A. J. Van Opstal, and A. Bernardino, "Modelling 3D saccade generation by feedforward optimal control," *PLOS Comput. Biol.*, vol. 17, pp. 1–35, 2021.
- [16] D. A. Robinson, "A quantitative analysis of extraocular muscle cooperation and squint," *Investig. Ophthalmol.*, vol. 14, pp. 801–825, 1975.
- [17] R. S. Snell and M. A. Lemp, *Clinical Anatomy of the Eye*. Hoboken, NJ, USA: Wiley, 2013.
- [18] D. A. Robinson and E. L. Keller, "The behavior of eye movement motoneurons in the alert monkey," *Bibl. Ophthalmol.*, vol. 82, pp. 7–16, 1972.
- [19] S. N. Kosari, S. Ramadurai, H. J. Chizeck, and B. Hannaford, "Control and tension estimation of a cable driven mechanism under different tensions," in *Proc. ASME Int. Des. Eng. Tech. Conf.*, vol. V06AT07A077, New York, NY, USA: ASME, 2013.
- [20] M. Haghighipanah, M. Miyasaka, and B. Hannaford, "Utilizing elasticity of cable-driven surgical robot to estimate cable tension and external force," *IEEE Robot. Autom. Lett.*, vol. 2, no. 3, pp. 1593–1600, Jul. 2017.
- [21] D. A. Robinson, "Modeling the oculomotor control system," *Prog. Brain Res.*, vol. 267, pp. 1–435, 2022.
- [22] F. C. Donders, "The 11th yearly report of the Netherlands Hospital for Necessitous Eye Patients (in Dutch)," Van de Weijer, Utrecht, The Netherlands, 1870, vol. 11.
- [23] D. Tweed and T. Vilis, "Implications of rotational kinematics for the oculomotor system in three dimensions," *J. Neurophysiol.*, vol. 58, pp. 832–849, 1987.
- [24] K. Hepp, "On Listings law," *Commun. Math. Phys.*, vol. 132, pp. 285–292, 1990.
- [25] A. J. Van Opstal, K. Hepp, B. J. M. Hess, D. Straumann, and V. Henn, "Two-rather than three-dimensional representation of saccades in monkey superior colliculus," *Science*, vol. 252, pp. 1313–1315, 1991.
- [26] T. Haslwanter, "Mathematics of three-dimensional eye rotations," *Vis. Res.*, vol. 35, pp. 1727–1739, 1995.
- [27] D. Tweed, B. Glenn, and T. Vilis, "Eye-head coordination during large gaze shifts," *J. Neurophysiol.*, vol. 73, pp. 766–779, 1995.
- [28] A. T. Bahill, M. R. Clark, and L. Stark, "The main sequence: A tool for studying human eye movements," *Math. Biosci.*, vol. 24, pp. 191–204, 1975.
- [29] J. A. M. Van Gisbergen, A. J. Van Opstal, and J. J. M. Schoenmakers, "Experimental test of two models for the generation of oblique saccades," *Exp. Brain Res.*, vol. 57, pp. 321–336, 1985.
- [30] S. K. Rajendran, Q. Wei, N. Yao, and F. Zhang, "Design, implementation, and observer-based output control of a super-coiled polymer-driven

- two degree-of-freedom robotic eye," *IEEE Robot. Autom. Lett.*, vol. 8, no. 9, pp. 5958–5965, Sep. 2023.
- [31] X. Y. Wang, Y. Zhang, X. J. Fu, and G. S. Xiang, "Design and kinematic analysis of a novel humanoid robot eye using pneumatic artificial muscles," *J. Bionic Eng.*, vol. 5, pp. 264–270, 2008.
- [32] M. Lakzadeh, "A biologically-inspired eye model for testing oculomotor control theories," Master's thesis, Univ. of British Columbia, Vancouver, BC, Canada, 2012. Accessed: Apr. 2012. [Online]. Available: <https://open.library.ubc.ca/collections/ubctheses/24/items/1.0072549>
- [33] Q. Wei, S. Sueda, and D. K. Pai, "Physically-based modeling and simulation of extraocular muscles," *Prog. Biophys. Mol. Biol.*, vol. 103, pp. 273–283, 2010.
- [34] A. Priamikov, M. Fronius, B. Shi, and J. Triesch, "OpenEyeSim: A biomechanical model for simulation of closed-loop visual perception," *J. Vis.*, vol. 16, pp. 25–25, 2016.
- [35] J. Iskander, M. Hosny, S. Nahavandi, and L. del Porto, "An ocular biomechanic model for dynamic simulation of different eye movements," *J. Biomech.*, vol. 71, pp. 208–216, 2018.
- [36] S. Schulz, S. M. zu Borgsen, and S. Wachsmuth, "See and be seen—rapid and likeable high-definition camera-eye for anthropomorphic robots," in *Proc. Int. Conf. Robot. Autom. (ICRA)*, 2019, pp. 2524–2530.
- [37] H. Liu, J. Luo, P. Wu, S. Xie, and H. Li, "Symmetric Kullback-Leibler metric based tracking behaviors for bioinspired robotic eyes," *Appl. Bionics Biomech.*, vol. 2015, pp. 1–11, 2015.
- [38] D. Dansereau, D. Wood, S. Montabone, and S. B. Williams, "Exploiting parallax in panoramic capture to construct light fields," in *Proc. IEEE Int. Conf. Robot. Autom. (ICRA)*, 2014, pp. 1–9.
- [39] N. F. Duarte, M. Rakovic, J. Tasevski, M. I. Coco, A. Billard, and J. Santos-Victor, "Action anticipation: Reading the intentions of humans and robots," *IEEE Robot. Autom. Lett.*, vol. 3, no. 4, pp. 4132–4139, Oct. 2018.
- [40] T. Kanda, H. Ishiguro, T. Ono, M. Imai, and R. Nakatsu, "Development and evaluation of an interactive humanoid robot 'Robovie,'" in *Proc. IEEE Int. Conf. Robot. Autom. (ICRA)*, vol. 2, Piscataway, NJ, USA: IEEE, 2002, pp. 1848–1855.
- [41] Y. Mohammad, S. Okada, and T. Nishida, "Autonomous development of gaze control for natural human-robot interaction," in *Proc. Workshop Eye Gaze Intell. Human-Mach. Interact.*, 2010, pp. 63–70.
- [42] E. S. Maini, L. Manfredi, C. Laschi, and P. Dario, "Bioinspired velocity control of fast gaze shifts on a robotic anthropomorphic head," *Auton. Robots*, vol. 25, pp. 37–58, 2008.
- [43] S. K. Rajendran, Q. Wei, and F. Zhang, "Two degree-of-freedom robotic eye: Design, modeling, and learning-based control in foveation and smooth pursuit," *Bioinspiration Biomimetics*, vol. 16, no. 4, 2021, Art. no. 046022.
- [44] M. R. C. Lucas, "Construction and characterization of a biomimetic robotic eye model with three degrees of rotational freedom: A testbed for neural control of eye movements," Master's thesis, Univ. Lisbon, Lisbon, Portugal, 2017.
- [45] R. Shadmehr and S. Mussa-Ivaldi, *Biological Learning and Control: How the Brain Builds Representations, Predicts Events, and Makes Decisions*. Cambridge, MA, USA: MIT Press, 2012, ch. 11.
- [46] A. F. Fuchs and E. S. Luschei, "Firing patterns of abducens neurons of alert monkeys in relationship to horizontal eye movement," *J. Neurophysiol.*, vol. 33, pp. 383–392, 1970.
- [47] A. F. Fuchs and E. S. Luschei, "The activity of single trochlear nerve fibers during eye movements in the alert monkey," *Exp. Brain Res.*, vol. 13, pp. 78–89, 1971.
- [48] K. Hepp and V. Henn, "Iso-frequency curves of oculomotor neurons in the rhesus monkey," *Vis. Res.*, vol. 25, pp. 493–499, 1985.
- [49] J. L. Demer, "Current concepts of mechanical and neural factors in ocular motility," *Curr. Opin. Neurol.*, vol. 19, pp. 4–13, 2006.
- [50] K.-M. Lee, A. P. Lai, J. Brodale, and A. Jampolsky, "Sideslip of the medial rectus muscle during vertical eye rotation," *Investig. Ophthalmol. Vis. Sci.*, vol. 48, pp. 4527–4533, 2007.
- [51] B. Dias, "Modeling, simulation, analytic linearization and optimal control of a 6 tendon-driven biomimetic eye: A tool for studying human oculomotor control," Master thesis, Jan. 2021.
- [52] J. M. Miller and D. A. Robinson, "A model of the mechanics of binocular alignment," *Comput. Biomed. Res.*, vol. 17, pp. 436–470, 1984.
- [53] J. Rychlewski, "On Hooke's law," *J. Appl. Math. Mech.*, vol. 48, pp. 303–314, 1984.
- [54] G. Wu and K. Sreenath, "Variation-based linearization of nonlinear systems evolving on SO(3) and S²," *IEEE Access*, vol. 3, pp. 1592–1604, 2015.
- [55] T. Lin, B. Horne, P. Tino, and C. Giles, "Learning long-term dependencies in NARX recurrent neural networks," *IEEE Trans. Neural Netw.*, vol. 7, no. 6, pp. 1329–1338, Nov. 1996.
- [56] H. Siegelmann, B. Horne, and C. Giles, "Computational capabilities of recurrent NARX neural networks," *IEEE Trans. Syst., Man, Cybern., B, Cybern.*, vol. 27, no. 2, pp. 208–215, Apr. 1997.
- [57] T. G. Thuruthel, E. Falotico, F. Renda, and C. Laschi, "Learning dynamic models for open loop predictive control of soft robotic manipulators," *Bioinspiration Biomimetics*, vol. 12, 2017, Art. no. 066003.
- [58] R. Shadmehr, J. J. O. De Xivry, M. Xu-Wilson, and T.-Y. Shih, "Temporal discounting of reward and the cost of time in motor control," *J. Neurosci.*, vol. 30, pp. 10507–10516, 2010.
- [59] L. Ljung, *System Identification: Theory for the User*, 2nd ed. Englewood Cliffs, NJ, USA: Prentice Hall PTR, 1999.
- [60] A. C. Smit and J. A. M. Van Gisbergen, "An analysis of curvature in fast and slow human saccades," *Exp. Brain Res.*, vol. 81, pp. 335–345, 1990.
- [61] A. J. Van Opstal and J. A. M. Van Gisbergen, "Scatter in the metrics of saccades and properties of the collicular motor map," *Vis. Res.*, vol. 29, pp. 1183–1196, 1989.
- [62] A. C. Smit, A. J. Van Opstal, and J. A. M. Van Gisbergen, "Component stretching in fast and slow oblique saccades in the human," *Exp. Brain Res.*, vol. 81, pp. 325–334, 1990.
- [63] Y. Suzuki, D. Straumann, J. I. Simpson, K. Hepp, and V. Henn, "Three-dimensional extra-ocular motoneuron innervation in the rhesus monkey. I: Muscle rotation axes and the on-directions during fixation," *Exp. Brain Res.*, vol. 126, pp. 187–199, 1999.
- [64] A. J. Van Opstal and J. A. M. Van Gisbergen, "Skewness of saccadic velocity profiles: A unifying parameter for normal and slow saccades," *Vis. Res.*, vol. 27, pp. 731–745, 1987.
- [65] C. S. Sherrington, *The Integrative Action of the Nervous System*. London, U.K.: Oxford Univ. Press, 1906.
- [66] D. A. Robinson, "The mechanics of human saccadic eye movement," *J. Physiol.*, vol. 174, pp. 245–264, 1964.
- [67] A. John, J. van Opstal, and A. Bernardino, "A cable-driven robotic eye for understanding eye-movement control," in *Proc. 9th Int. Conf. Autom., Robot. Appl. (ICARA)*, 2023, pp. 128–133.
- [68] R. Cardoso, "Feedback control on a model of a 3D biomimetic robotic eye," Master thesis, Instituto Superior Técnico, Lisbon, Portugal, 2019. Accessed: Dec. 2019. [Online]. Available: https://fenix.tecnico.ulisboa.pt/downloadFile/1689244997260701/thesis_finalissima.pdf



Reza Javanmard Alitappeh received the Ph.D. degree in AI and robotics from UFMG, Belo Horizonte, Brazil, in 2016.

He is an Assistant Professor with the University of Science and Technology of Mazandaran, Behshahr, Iran. He joined the ORIENT project with the Institute for Systems and Robotics (ISR) Instituto Superior Técnico (IST), Lisbon, Portugal. In 2019, he worked as a Research Fellow in autonomous vehicles with the Visual Artificial Intelligence Laboratory, Oxford Brookes University,

Oxford, U.K. His research interests include robotics, machine learning, and machine vision.



Akhil John (Student Member, IEEE) received the bachelor's degree in mechanical engineering, in 2018, and the master's degree in physics from BITS, Pilani, India, in 2018. He is currently working toward the Ph.D. degree with the Department of Electrical and Computer Engineering, Institute for Systems and Robotics (ISR), Instituto Superior Técnico (IST), Lisbon, Portugal. His Ph.D. research aims to study eye saccade control using a cable-driven robotic platform and use it for robotic vision.

He is a member of the VisLab at ISR. His research interests include mechanical design, control theory, computer vision, and neuroscience.



Bernardo Dias received the M.Sc. degree in electrical and computer engineering from the Instituto Superior Técnico (IST), Lisbon, Portugal, in 2020.

He was a Research Fellow with the Institute for Systems and Robotics (ISR), IST, for two years, where he developed the master thesis and research on modeling and controlling a six DoF biomimetic eye, designed according to the kinematics of the human eye.



A. John van Opstal received the Ph.D. degree, in 1989.

He is a Professor in biophysics with the Donders Center for Neuroscience, Radboud University Nijmegen, Nijmegen, The Netherlands. He studies and models neural sound-localization mechanisms, multisensory integration, and the neurophysiology of saccadic eye-head gaze shifts. He published more than 130 articles (GScholar: h-index 53) and the book titled *The Auditory System and Human Sound-Localization Behavior* (Elsevier, 2016). He advised 30 Ph.D. students.



Alexandre Bernardino (Senior Member, IEEE) received the Ph.D. degree, in 2004.

He is a Tenured Associate Professor and a Senior Researcher with the Institute for Systems and Robotics, IST, Lisbon University, Lisbon, Portugal. He published more than 300 research papers and participated in more than 20 national and international research projects, being the Principal Investigator in five of them. His main research interests include the application of computer vision, machine learning, cognitive science, and control theory to

advanced robotics and automation systems.